Performance Evaluation of Optical-Beam Stabilization Platforms With Different Supports Used in Large-Aperture Electro-Optical System

Yutang Wang , *Member, IEEE*, Ping Jia, Zhongshi Wang, Fuchao Wang, Songnian Tan , and Dapeng Tian , *Senior Member, IEEE*

Abstract—**Optical-beam stabilization platform (OBSP) provides high-precision inertial reference for measurement of full link optical-beam jitter in large-aperture electro-optical systems. To ensure that its optical-beam stability meets system alignment needs, performance evaluation of OBSP is necessary. Considering two OBSPs with flexible and rigid support, their optical-beam stability performance and effect on image quality are evaluated and compared via theoretical and experimental means. The results reveal that under same sensor and control algorithm conditions, the two OBSPs perform well on dynamic-frequency characteristics and two-axis motion decoupling, they can achieve dynamic optical-beam stabilization accuracy of $7.934\,\mu rad$ and $5.762\,\mu rad$ under $0.5–100\,Hz$ wide-band excitation, respectively. Moreover, optical systems equipped with OBSPs demonstrate better imaging performance (MTF value of 21% at 50 lp/mm with stable residuals of less than $7\,\mu rad$). The findings of this study provide a ready reference for the design of meter level large-aperture electro-optical systems for applications in laser communication, aerial imaging, etc.**

Index Terms—**Image quality, optical-beam jitter, optical-beam stabilization platform, optical-beam stability performance.**

I. INTRODUCTION

ELECTRO-OPTICAL systems play a critical role in numerous applications, such as remote sensing, space exploration, laser communication, aerial imaging, and other pertinent domains [1]–[3]. High-accuracy optical beam stabilization of large-aperture electro-optical systems remains a challenging task, especially under complex imaging environments [4]–[6].

The coarse-to-fine framework is a common way to realize optical beam stabilization in the presence of vibrations and disturbances [7], [8]. A gyro-feedback-based frame is applied as coarse stabilization for capturing and stabilizing a detecting target in the field of view. Moreover, a fast-steering mirror (FSM) is used as a fine stabilization means to achieve a fine adjustment of the optical beam [9]. However, in some cases, the aperture and focal length of electro-optical system increase to near or above the meter level to facilitate target detection over a range of hundreds of kilometers. In such cases, changes in the acceleration due to gravity and temperature, as well as external environment excitation, tend to deform the internal optical components and distort the optical beam throughout the optical path, which might severely deteriorate the resulting image quality and cannot be compensated for via conventional means.

An artificial optical-beam stabilization platform (OBSP) can address the abovementioned issues. Some airborne and satellite-based electro-optical systems, such as the stratospheric observatory for infrared astronomy and advanced land observing satellite, have employed an OBSP as a high-precision inertial reference to measure the optical-beam jitters [10], [11]. The OBSP, which is placed in the optical path of a large-aperture electro-optical system, is a compact installation with low drift, precise attitude determination, and wide-band dynamic characteristics. It provides a high-precision reference optical beam to mitigate optical-beam jitters in the electro-optical system.

The optical-beam stability performance of an OBSP is intimately associated with its support, by influencing the driving mode, sensor-space layout, platform size, and motion characteristics of the entire system. Based on the support type, OBSPs can be classified into two categories—flexible and rigid.

Owing to their compactness and high control accuracy, flexible supports have found broad applications in prior studies involving use of stabilization platforms with small apertures and light loads [12], [13]. An aluminium flexure for restoring mover position is designed and evaluated for a two-degree-of-freedom (2-DOF) hybrid-reluctance-force-based tip/tilt system [14]. [15] evaluates the performance of coherent free space optical communications with a FSM adaptive optics system. The relationship between system physics limits and system bandwidth is analyzed for a fast mirror system [16]. Whereas, these platform loads are supported by the flexible support,

unexpected micro-displacements along the non-working directions may be produced in a harsh environment, reducing the stabilization accuracy [17]. Moreover, such flexible supports are usually topped by a stiff reflector, thereby facilitating the dynamic stabilization performance over a wide frequency range [18]. For OBSPs, to measure the optical-beam jitter throughout the optical path in large-aperture electro-optical systems, inertial sensors and collimated optical source are required to be mounted on the upper part to provide a high-accuracy inertial reference optical-beam, which influences the performance of OBSP more complicatedly [19].

In addition to flexible supports, X–Y framework-based rigid supports are typically used in the design of mechanical gimbal for electro-optical systems owing to their advantages, including a large motion range and high loading capacity [20], [21]. A two-dimensional gimbal with adequate stiffness and high precision has been previously designed for use in inter-satellite laser-communication applications [22]. Multi-axial gimbal assemblies with 300-mm apertures have also been designed, and results of their finite-element structural analysis and fluid-flow dynamics have been reported [23]. In prior designs of the X–Y framework-based rigid supports for gimbals with large payloads, the nonlinear friction between the shafts has been found to limit their stabilization performance [24]. For example, the control bandwidth in such designs is generally limited to a few tens of Hertz. The introduction of a voice coil actuator (VCA) could reduce this shaft friction. However, the complex shaft structure, high rotational inertia, and low shaft accuracy of rigid supports directly influence system performance.

Many researchers have analyzed the performance of stabilization platforms with different supports from a variety of perspectives. The frequency responses and feedback performance were tested on a piezoelectric transducer (PZT)-actuated mirror [25]. From the perspective of control performance, five control algorithms were evaluated on the same FSM for addressing CMG induced jitter [26]. [27] compared the stabilization performance of three existing inertial-stabilization reference mechanisms. However, these platforms are designed with different mechanical structures and control schemes. Besides, the types of inertial sensors and corresponding noise treatment solutions used therein differ significantly. Furthermore, the influence of system vibration has been demonstrated by using modulation transfer function (MTF) to describe imaging degradation in [28], [29]. However, it remains unclear how OBSPs with distinct support structures differ in their optical-beam stability performance. Moreover, the impact of OBSP on the image quality of electro-optical systems should be investigated.

The proposed study comprehensively evaluates the optical-beam stability performance and effect on image quality of OBSPs equipped with different support types—(1) flexible support with a right circular flexure hinge and (2) X–Y frame-based rigid support. The main contributions of this study can be summarized as follows.

1) The optical-beam stability performance of OBSPs with flexible and rigid supports, in terms of their dynamic-frequency characteristics, motion performance, and wide-band dynamic stability performance, is analyzed and experimentally verified.
2) The influence of OBSPs on the image quality of electro-optical systems is theoretically analyzed and verified in terms of MTF. Additionally, a comprehensively design guidance for future OBSPs for meter level large-aperture electro-optical systems is provided.

The remainder of this paper is organized as follows. Section II presents a schematic of OBSPs employed in electro-optical systems. The design of OBSPs with flexible and rigid supports is presented in Section III. The performance evaluations and comparisons are presented in Section IV. Lastly, Section V discusses the findings of this study and highlights the major conclusions drawn thereof.

II. SCHEMATIC OF OPTICAL BEAM STABILIZATION PLATFORM IN LARGE-APERTURE ELECTRO-OPTICAL SYSTEMS

An OBSP is an essential all-on component in large-aperture electro-optical system for high-precision optical-beam stabilization, as depicted in Fig. 1. The OBSP mounted on the base of an electro-optical system comprises inertial sensors, actuators, and a collimated optical source, as well as other components. It maintains inertial stabilization during target acquisition, pointing, and tracking. As illustrated in the figure, the reference optical beam (marked in yellow in Fig. 1) from its collimated optical source passes through an extended corner cube to realize beam bending. Subsequently, it traces a path identical to that of the target optical beam (marked in orange in Fig. 1), passes through an optical splitter, projects onto an alignment sensor, and facilitates the measurement of the total jitter in the optical path. Because the OBSP is mounted on the same base as the primary mirror of the electro-optical system, and the base is rigidly connected to the entire system, the jitter of the target optical beam caused by the deformation of optical components in the optical path could be measured. Thereafter, the output of this sensor is feedback to a FSM to calibrate the target optical beam for high-precision optical-beam stabilization.

The introduction of the OBSP calibrates the beam jitter caused by the non-rigidity of the system's optical-mechanical structure. The extent to which it affects the image quality depends on the degree of dispersion of the image point on the image plane. Focusing on optical-beam propagation inside the optical system, to evaluate the effect of OBSP on the image quality of the entire electro-optical system, the MTF is presented as a metric to describe the optical properties of the optical system as a function of the spatial frequency. This facilitates an objective evaluation of the image quality and has important implications for the design of the entire optical system.

Generally, the non-rigidity of the optical-mechanical structure leads to random vibrations of the internal optical components in the electro-optical system, which cause jittering of the optical beam. Without an OBSP, the random vibration will act on the image plane, resulting in the dispersion of image points. When an OBSP is equipped, only the stable residuals of the optical-beam may affect the image point on the image plane, which will be
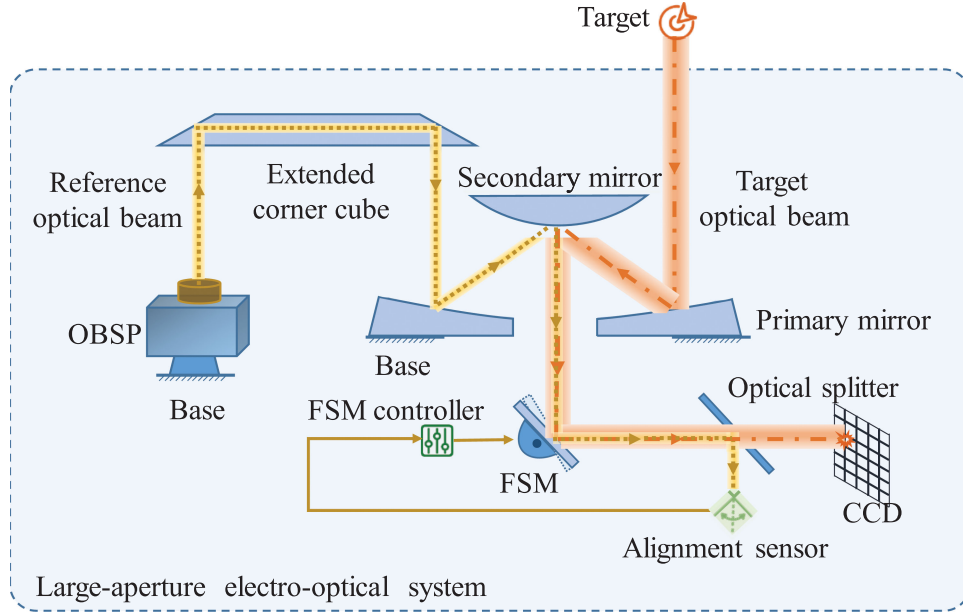
Fig. 1. Diagram of Large-aperture electro-optical system with OBSP.

much smaller than in the previous case. In principle, these image points are blurred into Gaussian patterns, and the root mean square (RMS) value of the dispersion displacement σ on the image plane is related to the final jitter angle of the optical beam θ_i as follows:

$$\sigma = f' sin(\theta_i), \tag{1}$$

where f' denotes the focal length of the optical system.

The resulting line spread function (LSF) induced by random vibrations is expressed as

$$LSF = -\frac{1}{\sqrt{2\pi}\sigma}exp\left(\frac{x^2}{2\sigma^2}\right), \tag{2}$$

where x denotes the spatial coordinate. By applying the Fourier transform to the LSF, the MTF can be expressed as

$$
\begin{aligned}
MTF(f_s) &= \left| \int_{-\infty}^{+\infty} -\frac{1}{\sqrt{2\pi}\sigma}exp\left(-\frac{x^2}{2\sigma^2} - 2\pi i f_s x\right)dx \right| \\
&= exp(-2\pi^2\sigma^2 f_s^2) \\
&= exp(-2\pi^2 sin^2(\theta_i)f'^2 f_s^2), \tag{3}
\end{aligned}
$$

where f_s denotes the spatial frequency.

III. DESIGN OF OBSPs EQUIPPED WITH DIFFERENT SUPPORT STRUCTURES

A. OBSP With a Flexure-Hinge Support

The OBSP with a flexure-hinge support (OBSP-FH) comprises a collimated optical source, fiber optic gyros, position proximity sensors, VCAs, and a flexure hinge among other components (Fig. 2). The gyros and collimated optical source are placed on the upper plate of the platform and are connected to the base through a two-axis flexure hinge.
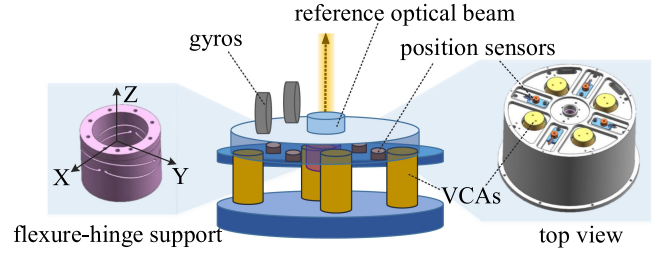

Fig. 2. Design drawing of OBSP with flexure-hinge support.

VCAs are chosen instead of piezoelectric actuators for OBSP-FH, considering the OBSP design requirements of motion range, working environment, and structural characteristics. In our design, the motion range of the OBSP needs to be greater than $\pm 3.5\,mrad$, which corresponds to a displacement of more than $1mm$ in the direction of actuator movement. In the compact design space of the OBSP, it is difficult to place a piezoelectric actuator with a stroke exceeding $100\,\mu m$. Besides, considering the working gap between the magnetic base and the coil of VCA, VCA is more suitable for the harsh working environment and structural compactness of the OBSP. Further, because the VCA magnet mass exceeds the coil mass, the VCA coil and magnet are fixed to the upper and lower plates, respectively. This reduces the rotational inertia of the moving OBSP parts and increases the control bandwidth. Four VCAs and position proximity sensors each are evenly distributed in a cross configuration to ensure platform miniaturization. Each VCA pair operates in differential mode to realize dual-axis movement.

The flexible OBSP-FH support represents a decoupled 2-DOF flexible support comprising a right circular flexure hinge. It utilizes the small angular deformation and self-recovery property of an elastic material to realize micro-displacements. This support
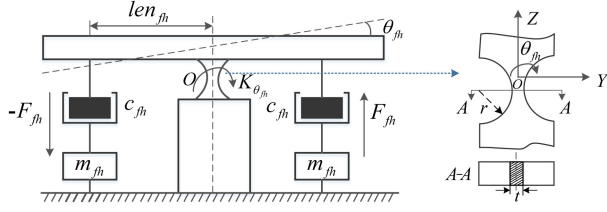
Fig. 3. Structure diagram of optical beam stabilization platform with flexure hinge.

Fig. 4. Design drawings of OBSP with X–Y framework-based rigid support.

structure offers appropriate operational flexibility and high stiffness in the working and non-working directions, respectively. This structure can be machined integrally to avoid assembly errors. Furthermore, the elimination of gaps and friction facilitates the realization of high-precision movements and increases the structural stiffness of the system. In summary, the OBSP-FH structure is compact, frictionless, and highly responsive. These characteristics warrant its deployment in OBSPs with a small angular displacement and high-precision rotation.

Two of the four VCAs and position sensors in the above-described OBSP-FH operate in coordination to actuate the platform and measure the corresponding angular information with the same amplitude and in opposite direction. This further improves the zero stability of the OBSP-FH configuration and reduces the measurement threshold by differentiating the measured values.

The simplified dynamic model of the OBSP-FH is shown in Fig. 3. The motion of this support structure is decoupled along both the x- and y-axes; the following analysis considers the x-axis alone. The force equilibrium equation for the OBSP-FH structure along the x-axis can be expressed as

$$2len_{FH}F_{FH} = (K_{FH} + 2K_{t_{FH}})\theta_{FH}$$
$$= K_{\theta_{FH}}\theta_{FH}, \qquad (4)$$

where len_{FH} denotes the distance from the point of VCA force action to the OBSP-FH rotational axis; θ_{FH} denotes the motion angle of the OBSP-FH; F_{FH} denotes the VCA force; $F_{FH} = i_{FH}k_{c_{FH}}$, i_{FH} is the electric current; and $k_{c_{FH}}$ denotes the force constant. Additionally, K_{FH} denotes the equivalent rotational stiffness of the flexure hinges, $K_{t_{FH}} = M_{t_{FH}}/2\theta_{FH}$ denotes the torsional stiffness caused by the structure aligned with the x-axis, and $M_{t_{FH}}$ represents the angular moment caused by the structure in the y-axis when the upper part of the OBSP-FH tilts about the x-axis. Lastly, $K_{\theta_{FH}}$ denotes the rotational stiffness of the flexible support.

The torque balance equation is expressed as

$$M_{FH} = [J_{FH} + 2m_{fh}len^2_{FH}]\ddot{\theta}_{FH}$$
$$+ 2c_{FH}len^2_{FH}\dot{\theta}_{FH} + K_{\theta_{FH}}\theta_{FH}, \qquad (5)$$

where M_{FH} represents the control torque; J_{FH} denotes the load inertia of the upper part of the OBSP-FH, as well as the corresponding holder; m_{FH} denotes the mass of the moving coil along with the connecting part; and c_{FH} denotes the equivalent damping of the VCA and support structure along the x-axis.
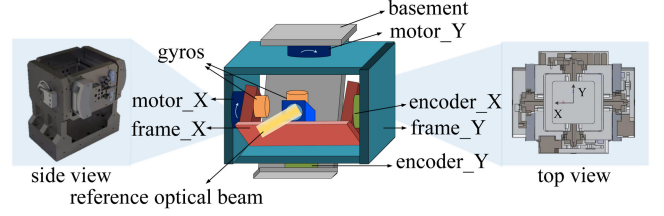
According to Kirchhoff's law, the actuator voltage can be expressed as

$$u_{FH} = L_{FH}\dot{i}_{FH} + R_{FH}i_{FH}, \qquad (6)$$

where u_{FH} denotes the VCA control voltage along the x-axis. L_{FH} and R_{FH} denote the VCA inductance coefficient and corresponding resistance, respectively.

The relationship between M_{FH} and i_{FH} is given by

$$M_{FH} = 2i_{FH}k_{c_{FH}}len_{FH}. \qquad (7)$$

Combining (5)–(7), the OBSP-FH transfer function from the control voltage to the output angle about the x-axis can be expressed as

$$G_{FH}(s) = \frac{\theta_{FH}(s)}{U_{FH}(s)}$$
$$= \frac{2k_{c_{FH}}L_{FH}}{(J'_{FH}s^2 + 2c_{FH}len^2_{FH}s + K_{\theta_{FH}})(L_{FH}s + R_{FH})}. \qquad (8)$$

where $J'_{FH} = J_{FH} + 2m_{FH}len^2_{FH}$.

B. OBSP with an X–Y Framework-Based Rigid Support

The OBSP equipped with an X–Y framework-based rigid support (OBSP-XY) comprises the X and Y frames, shafting mechanism, VCAs as drive mechanism, as well as gyros and optical encoders for motion-information measurement. The collimated optical source is internally mounted within the frames. Fig. 4 illustrates the OBSP-XY setup.

Considering the decupled motion of the OBSP-XY setup in the X direction alone, the system dynamics can be expressed as

$$R_{XY}i_{XY} + L_{XY}\frac{di}{dt} + K_{e_{XY}}\dot{\theta}_{XY} = u_{XY}, \qquad (9)$$

$$M_{XY} = K_{t_{XY}}i_{XY}, \qquad (10)$$

$$J_m\ddot{\theta}_{XY} + B_m\dot{\theta}_{XY} = M_{XY} + M_i, \qquad (11)$$

where R_{XY} denotes the armature resistance, i_{XY} denotes the electric current, L_{XY} denotes the armature inductance, $K_{e_{XY}}$ denotes the back-EMF coefficient, θ_{XY} denotes the rotation angle, u_{XY} represents the armature voltage, M_{XY} represents the motor-output torque, $K_{t_{XY}}$ denotes the electromagnetic torque constant, J_m denotes the rotating inertia, B_m denotes the damping coefficient, and M_i denotes the shaft disturbance.

Key parameters	OBSP-FH	OBSP-XY
Type of support structure	flexible support, flexure hinge	rigid support, X-Y framework
Maximum angular range($mrad$)	$\geq \pm 4.54$ (X,Y axis)	$\geq \pm\ 102.2$ (X,Y axis)
Mechanism size(mm)	$\Phi 208 \times 178$	$216 \times 175 \times 185$
Mechanism mass(kg)	4.988	6.95
Type of drive motor	rotary voice coil actuator	cylindrical voice coil actuator
Peak torque(Nm)	1.08	1.2
Type of inertial angular velocity sensor	fiber-optic gyro	fiber-optic gyro
Velocity measurement resolution($\mu rad/s$)	1.17	1.17
Type of position sensor	eddy current sensor	miniature circular grating
Position measurement resolution(μrad)	0.17	8.72

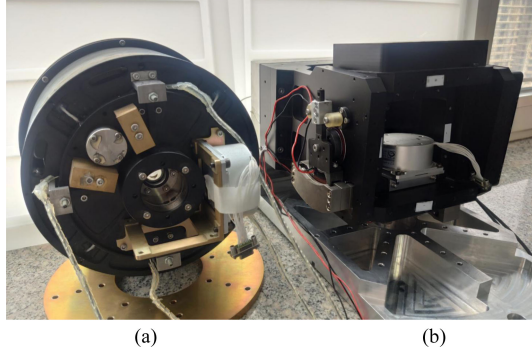Fig. 5. Experimental instruments: (**a**) OBSP-FH; (**b**) OBSP-XY.

(a)

(b)

Fig. 6. Experimental setups: (**a**) OBSP-FH; (**b**) OBSP-XY.

Combining (9)–(11), the electromechanical model of the OBSP-XY can be expressed as

$$J_m \ddot{\theta}_{XY} + B_m \dot{\theta}_{XY} = \frac{K_{t_{XY}}}{R_{XY}} \left(u_{XY} - K_{e_{XY}} \dot{\theta}_{XY} - L_{XY} \frac{dM_{XY}}{dt} \right) + M_i. \quad (12)$$

In general, the armature inductance in the OBSP-XY structure is small. Considering the dynamics induced by the armature inductance as part of the disturbance, the order of the control terms in (12) can be reduced. Accordingly, the equation can be simplified by setting $J_{XY} = R_{XY} J_m / K_{t_{XY}}$, $B_{XY} = (R_{XY} B_m + K_{e_{XY}} K_{t_{XY}})/K_{t_{XY}}$, and $M_{d_{XY}} = R_{XY} M_i / K_{t_{XY}} - L_{XY} \frac{dM_{XY}}{dt}$. The resulting differential equation can be expressed as

$$J_{XY} \ddot{\theta}_{XY} + B_{XY} \dot{\theta}_{XY} = u_{XY} + M_{d_{XY}}. \quad (13)$$

Notably, when disregarding $M_{d_{XY}}$, the transfer function of the OBSP-XY from the control voltage to the output angle around the x-axis can be expressed as

$$G_{XY}(s) = \frac{\theta_{XY}(s)}{U_{XY}(s)} = \frac{1}{J_{XY} s^2 + B_{XY} s}. \quad (14)$$

IV. PERFORMANCE-EVALUATION EXPERIMENTS AND ANALYSIS

A. Experimental Setup

According to the block diagrams of the design structure in Fig. 2 and Fig. 4, the designed OBSP-FH and OBSP-XY are shown in Fig. 5 and their key parameters are listed in Table I.
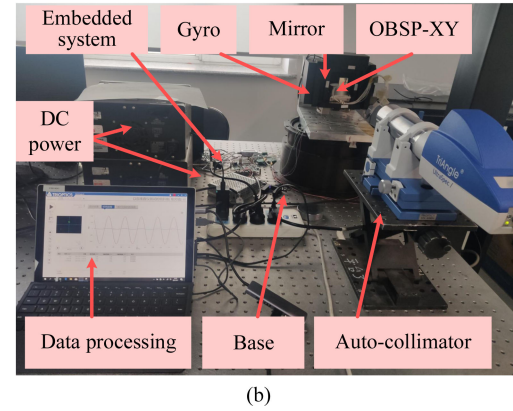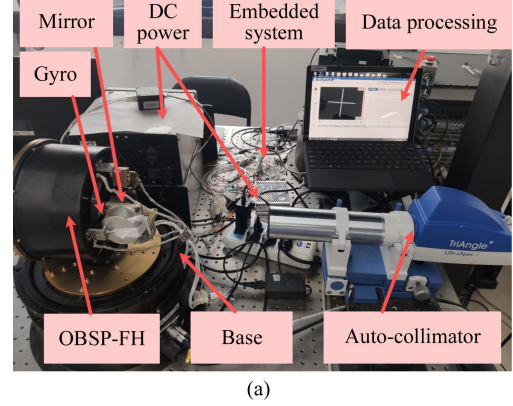
During the structural design, to achieve a lightweight design and meet the working requirements of a harsh mechanical vibration environment, the structure materials of the OBSP-FH and OBSP-XY are selected for their low density, high stiffness and strength. Analyzing parameters such as material densities, thermal conductivity, specific stiffness, and coefficient of linear expansion, aluminium alloys were chosen as the main structural materials and titanium alloys were chosen for the flexible support.

Additionally, both experimental setups are illustrated in Fig. 6 to verify the performance of the OBSP-FH and OBSP-XY. The control algorithms for the two configurations were directly ported to a microcontroller (MCU)-embedded control system. The control value was output to a linear amplifier operating as the motor driver through a digital-to-analog (DA) converter. The same fiber-optic gyros with a random wandering coefficient of
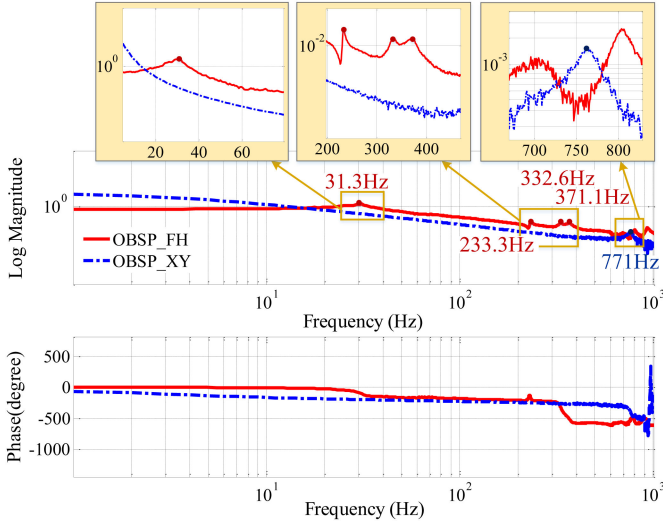
Fig. 7.   Frequency-response curves of the OBSP-FH and OBSP-XY.

less than $0.0025°/\sqrt{h}$ were fixed on both OBSPs for measuring the angular velocity signals in the inertial space. The analog gyro and encoder signals are converted to their digital equivalent using an analog-to-digital (AD) converter.

To generate a wideband dynamic-excitation signal, both OBSPs were mounted on identical rotatable bases. The resolution of the optical-electricity encoder was set to $0.00007°$. The control algorithms of the bases were scripted in C language and implemented on a Linux-based real-time system with a GCC environment installed on an industrial personal computer (Advantech IPC-610L).

Prior to performing the comparison experiments, the axes of both OBSPs were calibrated using a high-precision autocollimator (TriAngle UltraSpec). A $25.4 \times 25.4\,mm$ silver-coated metallic mirror was mounted on both OBSPs, thereby forming an axis perpendicularity detection and calibration system equipped with an autocollimator. This minimizes the errors induced by the optical-machine setup of the OBSPs.

B. DynamiC-Frequency Characteristics of the OBSPs

This test is aimed at verifying the dynamic-frequency characteristics observed owing to the inherent structural properties of the two OBSPs, including the amplitude- and phase-frequency characteristics. Specifically, a section of the pseudo-random noise was generated as an excitation signal and output via the DA module to the OBSP. Subsequently, the open-loop frequency characteristics of both OBSPs were identified via spectral analysis performed based on the recorded excitation signal and the corresponding system response signal. The inherent resonant frequencies of the OBSPs corresponding to the occurrence of the peak amplitude could be determined by observing the corresponding amplitude–frequency characteristic curves.

Fig. 7 depicts the dynamic frequency-response curves obtained for both OBSPs. By performing curve fitting in accordance with the obtained OBSP frequency-response data, the OBSP-FH transfer function from control voltage to output angle

can be expressed as (15).

$$G_{FH}(s) = \frac{\theta_{FH}(s)}{U_{FH}(s)}$$

$$= \frac{1}{0.0000000049s^3 + 0.000049s^2 + 0.0027s + 1.87}.$$
(15)

The corresponding OBSP-XY transfer function is given by

$$G_{XY}(s) = \frac{\theta_{XY}(s)}{U_{XY}(s)} = \frac{1}{0.00014s^2 + 0.001s}.$$
(16)

This confirms that the transfer function form corresponding to the OBSP-FH (15) and OBSP-XY configurations (16) is consistent with the form of those derived in Section 3–i.e., (8) and (14), respectively.

As can be seen from the amplitude-frequency curve in Fig. 7, the first four natural frequencies of the OBSP-FH configuration are 31.3, 233.3, 332.6 and $371.1\,Hz$, whereas the main natural frequency of the OBSP-XY setup is $771\,Hz$. From the phase-frequency curve, the phase lag of both OBSPs generally increases with frequency. The phase lag of the OBSP-FH is smaller when the signal frequency f_t is below $20\,Hz$ and the total phase lag is greater than that of OBSP-XY, this is due to the fact that the flexure-hinge support is a virtually frictionless, spring-damper structure with a transfer function as (15). In addition, owing to the inherent characteristics of the flexible hinge, the OBSP-FH configuration demonstrates underdamping characteristics, which cannot prevent the vibrations from crossing the equilibrium position back and forth. In addition, because the OBSP-FH structure is characterized by multiple natural frequencies that exceed $200\,Hz$, it is difficult to realize wide-bandwidth control in this case compared to that involving the OBSP-XY. In this study, the influence of different supports on OBSP performance was objectively evaluated using the proportional-integral-derivative (PID) control algorithm as a closed-loop controller and the disturbance observer (DOB) as the disturbance estimator.

C. Motion Performance

1) Movement Relationship Between Input Voltage and Motion Range: In this study, the motion relationships between the OBSP input and output was evaluated by performing a set of closed-loop motion tests. In these tests, the OBSPs were moved in accordance with a triangular wave command. The results obtained are depicted in Fig. 8.

As can be observed in Fig. 8(a), the OBSP-FH output angle lies in the -4–$4\,mrad$ range when the driving voltage is $\pm0.4V$. In general, the output angle demonstrates an approximately linear trend corresponding to changes in the input voltage. This can be attributed to the characteristics of the flexure hinge. Therefore, the OBSP-FH configuration is nearly immune to disturbance during motion. The low nonlinearity and the observed difference in the output angle can be mainly attributed to the machining and assembling errors of the mechanical structure. For the OBSP-XY configuration, as shown in Fig. 8(b), the output angle lies in the -85–$85mrad$ range when the driving
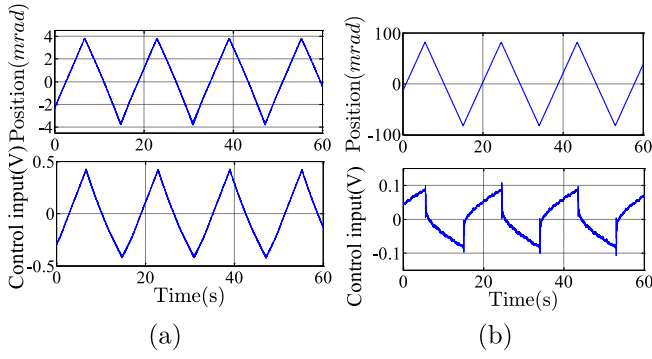
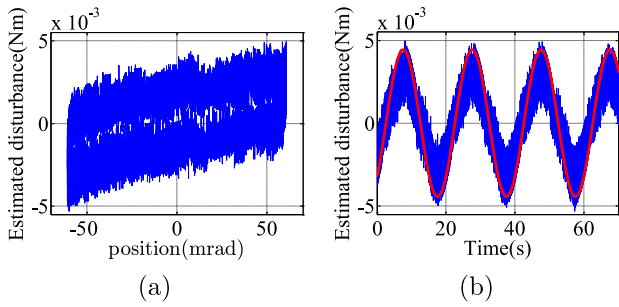Fig. 8.   Motion relationship between input voltage and motion range: (**a**) OBSP-FH; (**b**) OBSP-XY.

Fig. 9.   Estimated disturbance and data fitting (**a**) Curve of position response and estimated disturbance; (**b**) Estimated and fitted shaft disturbance.

voltage is $\pm 0.1V$. However, there exists an evident nonlinearity in the control input to the OBSP-XY configuration under the linear-motion command.

In the OBSP-XY configuration, the movement around the shafts causes additional disturbance, which must be compensated for by the DOB. In this study, this compensation was quantitatively verified by applying an open-loop DOB to the OBSP-XY configuration to estimate the corresponding shaft disturbance. By making the OBSP-XY setup perform a slow reciprocating motion at uniform speed, the DOB could estimate the shaft disturbance based on the control command and position response of the encoder. Fig. 9 depicts the results of the estimated disturbance in different horizontal coordinates. It can be observed that the shaft disturbance in the OBSP-XY configuration is small, but varies sinusoidally, as opposed to classical friction models such as the Lugre or Stribeck friction models.

The shaft disturbance observed in the OBSP-XY configuration can be simplified as an elastic moment around the equilibrium point expressed as

$$M_{d_w} = A_w k_w sin \left(\frac{\sqrt{(k_w)^2 - \frac{c_w^2}{4}}}{J_w q_0} \theta_{xy} + \phi_w \right) \qquad (17)$$

where J_w, c_w, k_w denote the moment of inertia, damping, and stiffness coefficients, respectively, for generating the elastic moment. Moreover, A_w and ϕ_w are parameters related to the motion differential equations and the initial OBSP-XY state.
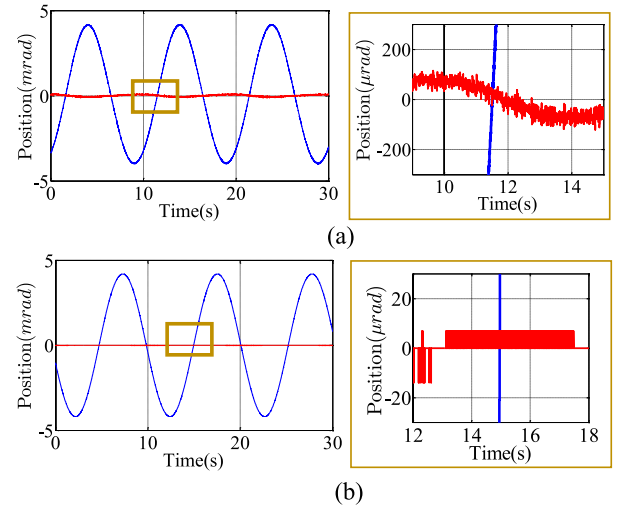

Fig. 10.   Two-axis decoupling performance: (**a**) OBSP-FH; (**b**) OBSP-XY.

By fitting the curve depicted in Fig. 9(b), the elastic shaft disturbance in the OBSP-XY configuration can be expressed as $M_{d_w} = 0.00444sin(0.00031416\theta_{xy} - 0.8116)$. The maximum value of this expression is much smaller compared to the OBSP-XY motor torque listed in Table I.

2) Two-Axis Motion Decoupling Performance: As already stated, optical-beam jitters in electro-optical systems cause image-quality degradation along both the x and y directions of the charge-coupled device. To facilitate an accurate optical-beam jitter compensation, it is necessary to ensure that OBSP motions along both its dimensions are decoupled to the extent possible. Accordingly, in this study, two-axis OBSP motion decoupling tests were performed to evaluate their decoupling performance. In these tests, the OBSP structure along one axis was subjected to fixed-amplitude sinusoidal oscillations, whereas that along the other axis was maintained static.

As depicted in Fig. 10, the maximum coupling of the OBSP-FH configuration about the y-axis is 3.1%, whereas that of the OBSP-XY configuration is 0.25%. This indicates that the OBSP-XY setup demonstrates excellent two-axis decoupling performance, whereas the mechanical process of the 2-DOF right circular flexure hinge in the OBSP-FH setup makes it difficult to guarantee the realization of a rigid kinematic structure. Therefore, the decoupling performance of the OBSP-FH setup is less favorable compared to that of its OBSP-XY counterpart. To achieve better decoupling performance, an additional control strategy should be introduced to suppress the coupling effect between axes.

D. Performance Evaluation of the Optical-Beam Dynamic Stability Under Mechanical Vibration

1) Dynamic Stability Performance Under 0.5–100 Hz Wide-Band Random Continuous Dynamic Excitation: Electro-optical systems invariably operate under harsh environments characterized by complex vibrations and disturbances distributed over a wide frequency band. In this study, the optical-beam
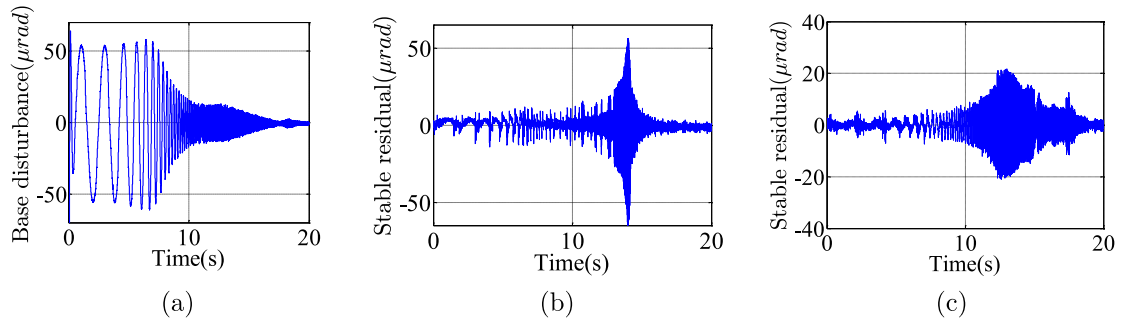
Fig. 11. Dynamic stability under 0.5–100 Hz dynamic excitation: (**a**) 0.5–100 Hz dynamic vibrations generated by the rotatable base; (**b**) Inertial stable residuals of OBSP-FH (**c**) Inertial stable residuals of OBSP-XY.

TABLE II
OPTICAL-BEAM STABILITY PERFORMANCE COMPARISON BETWEEN OBSP-FH AND OBSP-XY

Parameters	OBSP-FH	OBSP-XY
First-order resonance frequency	31.3Hz	771Hz
Order of transfer function	Third order	Second order
Relationship between motion range and input voltage	nearly linear	existing small nonlinearity
Structural friction	not obvious	little elastic disturbance
Maximum motion coupling ratio of the two axes	3.1%	0.25%
Inertial stable residual under 0.5–100Hz vibration	$7.9342\mu rad$	$5.762\mu rad$

dynamic-stability performance of the two candidate OBSPs was evaluated by performing a set of experiments, wherein OBSPs were mounted on identical rotatable bases that generate random continuous sweep vibrations over the $0.5–100\,Hz$ range. The corresponding absolute vibration amplitude decreases from more than $100\,mrad$ to zero.

Fig. 11 depicts the curves corresponding to the base disturbance and inertial stable residuals of OBSPs, thereby demonstrating the robustness of both OBSPs to base vibrations. The RMS values of the stable residuals corresponding to the OBSP-FH and OBSP-XY configurations subjected to band disturbances in the 0.5–100 Hz range were statistically analyzed to equal 7.9342 and $5.762\,\mu rad$, respectively.

Furthermore, it can be noted that there is a spike in stable residual in Fig. 11(b), which indicates there is a OBSP-FH resonance point at the corresponding frequency point that has not been suppressed. As described in the analysis of the dynamic-frequency characteristics of OBSPs, due to the structure characteristics of flexure-hinge support, there are more resonance points for the OBSP-FH in more relatively low frequency bands. However, for a more reasonable performance comparison between the OBPS-FH and OBSP-XY configurations, we applied the same control frame and sensors in our experiments. If full suppression is desired, an additional design of notch filter for this resonant frequency may be required.

2) Dynamic Stability Performance of the Optical-Beam Under Dynamic Excitation at Different Frequencies: A further set of experiments were performed to investigate the optical-beam dynamic-stability performance of the two OBSPs subjected to dynamic excitation at different signal frequencies f_t in a range of 1–100 Hz. In these experiments, the rotatable base generated a set of sinusoidal excitation signals of fixed frequencies, and the corresponding RMS stable residuals for both OBSPs were recorded. The results obtained are presented in Fig. 12. As can
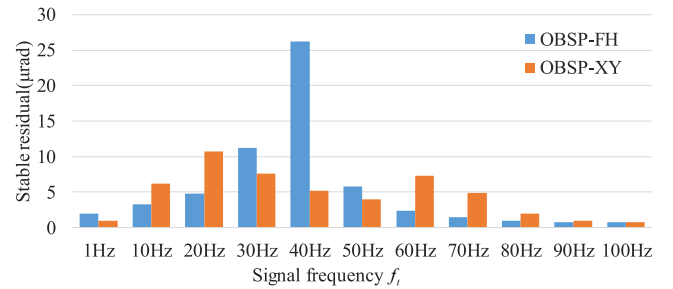

Fig. 12. Dynamic-stability performance evaluated under dynamic excitations at different signal frequencies.

be seen, these experimental results are consistent with those described in the previous section. Notably, these results demonstrate the dynamic stability performance of both OBSPs more clearly. It can be inferred that the OBSP-FH setup resonates at approximately 40 Hz, whereas its OBSP-XY counterpart resonates at approximately 20 Hz.

In general, Table II summarizes the results of the above-described analyses and evaluation of the optical-beam stability properties of the OBSPs. As can be seen from the data in Tables I and II, the OBSP-FH affords the advantages of low platform weight and small size with low structural friction, whereas with greater motion coupling between the two axes and smaller motion range. Moreover, because the system frequency response of OBSP-FH demonstrates undamped characteristics, it is difficult to improve its control-gain in its closed-loop systems. Conversely, the OBSP-XY demonstrates high structural rigidity and load capacity with a wider range of motion. In addition, the first-order intrinsic frequency of the OBSP-XY setup is sufficiently high to achieve a high control gain; therefore, the resulting optical-beam stability performance is superior to OBSP-FH under the same control framework. However, the
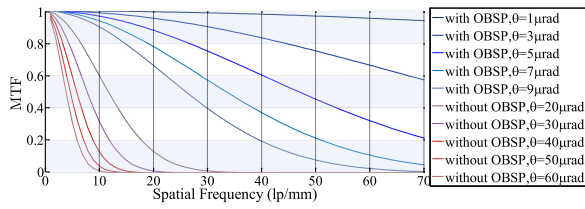
Fig. 13. Influence of random vibrations on image quality of electro-optical systems.

OBSP-XY setup is characterized by the inevitable friction between shafts even with VCAs. Moreover, this configuration is characterized by high platform weight and large size.

E. Performance Influence of the OBSP on Image Quality in Electro-Optical Systems

This subsection discusses the influence of random vibrations on the image quality in electro-optical systems with and without an OBSP. For large-aperture electro-optical systems with a focal length of $0.8\,m$ and a detector pixel size of $9\,\mu m$, if the jitter of the optical beam without an OBSP is $20, 30, 40, 50, 60\,\mu rad$ and the jitter residual of the optical beam with an OBSP is $1, 3, 5, 7, 9\,\mu rad$, respectively, the MTF curves according to (3) are shown in Fig. 13.

Fig. 13 reveals that the image quality of a large-aperture electro-optical system without an OBSP deteriorates quickly, and the corresponding MTF values drops below 0.2 when the spatial frequency is less than $20\,lp/mm$. The OBSP compensates for the optical-beam jitter throughout the optical path of the electro-optical system. Accordingly, an electro-optical system with an OBSP can resolve spatial frequencies of $50\,lp/mm$ or more when the value of the stable inertial residuals is less than $7\,\mu rad$. This satisfies the imaging requirements in accordance with the expression used for calculating the spatial frequency. High-performance OBSPs are essential components of large-aperture electro-optical systems and facilitate the attainment of high-quality imaging.

V. CONCLUSION

In summary, we have comprehensively evaluated and compared the optical-beam stability performance and effect on imaging quality of OBSPs with different supports. Both OBSP structures considered in this study demonstrate excellent optical-beam-stabilization capabilities, including dynamic-frequency characteristics, motion performance and wide-band dynamic stability performance, which are consistent with the theoretical analysis in Section III. For the OBSP-FH, an additional trap filter should be introduced for suppressing its low-frequency resonance caused by underdamping to obtain better optical-beam stability performance. It can be inferred that the OBSP-FH structure is more suitable for use in applications involving limited space availability and those that require high absolute-position accuracy. Meanwhile, the OBSP-XY structure is more suited for applications that require a large motion range and low axis coupling.

Due to the limitation of component distribution and structural stiffness, the structural dimensions of the OBSP-FH and OBSP-XY in this study are still relatively large and difficult to apply in a wider range of electro-optical systems. In future work, we will investigate more compact OBSPs that combine the merits of both the OBSP-FH and OBSP-XY configurations. For example, introducing more miniaturized sensors and light sources, using magnetic bearings as supports to reduce the size of the OBSP to some extent, introducing high-precision position sensors to improve the stabilization accuracy of the OBSP-FH in OBSP-XY configurations, and removing the inertial sensors of the upper plate of the OBSP-FH to be fixed to the base of the EO system with feed-forward control to further optimize the OBSP structure design, etc.

REFERENCES

[1] Y. Kaymak, R. Rojas-Cessa, J. Feng, N. Ansari, and M. Zhou, "On divergence-angle efficiency of a laser beam in free-space optical communications for high-speed trains," *IEEE Trans. Veh. Technol.*, vol. 66, no. 9, pp. 7677–7687, Sep. 2017.

[2] L. Jiang and X. Yang, "Study on enlarging the searching scope of staring area and tracking imaging of dynamic targets by optical satellites," *IEEE Sensors J.*, vol. 21, no. 4, pp. 5349–5358, Feb. 2021.

[3] O. Cierny and K. L. Cahoy, "On-orbit beam pointing calibration for nanosatellite laser communications," *Opt. Eng.*, vol. 58, no. 4, 2018, Art. no. 041605.

[4] M. Zhang, B. Li, and S. Tong, "A new composite spiral scanning approach for beaconless spatial acquisition and experimental investigation of robust tracking control for laser communication system with disturbance," *IEEE Photon. J.*, vol. 12, no. 6, Dec. 2020, Art. no. 7906212.

[5] Q. Li, L. Liu, X. Ma, S. Chen, H. Yun, and S. Tang, "Development of multitarget acquisition, pointing, and tracking system for airborne laser communication," *IEEE Trans. Ind. Informat.*, vol. 15, no. 3, pp. 1720–1729, Mar. 2019.

[6] J. Zhang, "A review of common-path off-axis digital holography: Towards high stable optical instrument manufacturing," *Light: Adv. Manuf.*, vol. 2, no. 23, pp. 333–349, 2021.

[7] B. Xiang and Q. Mu, "Gimbal control of inertially stabilized platform for airborne remote sensing system based on adaptive RBFNN feedback model," *IFAC J. Syst. Control*, vol. 16, 2021, Art. no. 100148.

[8] V. K. Kappala, J. Pradhan, A. K. Turuk, V. N. H. Silva, S. Majhi, and S. K. Das, "A point-to-multi-point tracking system for FSO communication," *IEEE Trans. Instrum. Meas.*, vol. 70, Sep. 2021, Art. no. 5504110, doi: 10.1109/TIM.2021.3115202.

[9] C. Deng, T. Tang, Y. Mao, and G. Ren, "Enhanced disturbance observer based on acceleration measurement for fast steering mirror systems," *IEEE Photon. J.*, vol. 9, no. 3, Jun. 2017, Art. no. 6802211.

[10] H. Li, Y. Yang, P. Jia, and Y. Wang, "Application of active disturbance rejection control in tracking problem of IPSRU," in *Proc. 12th IEEE Int. Conf. Control Automat.*, 2016, pp. 616–620.

[11] J. P. Gilmore, M. F. Luniewicz, and D. G. Sargent, "Enhanced precision pointing jitter suppression system," in *Proc. Laser Beam Control Technol.*, 2002, pp. 38–49.

[12] D. Li, T. Wu, Y. Ji, and X. Li, "Model analysis and resonance suppression of wide-bandwidth inertial reference system," *Nanotechnol. Precis. Eng.*, vol. 2, no. 4, pp. 177–187, 2019.

[13] X. Xu, G. Zhang, and C. Chen, "Design and performance test of the fast-steering mirror with flexure hinge used in vehicle track-launch system," *Optoelectron. Lett.*, vol. 15, no. 3, pp. 179–184, May 2019.

[14] E. Csencsics, J. Schlarp, and G. Schitter, "High-performance hybrid-reluctance-force-based tip/tilt system: Design, control, and evaluation," *IEEE/ASME Trans. Mechatronics*, vol. 23, no. 5, pp. 2494–2502, Oct. 2018.

[15] W. Liu, K. Yao, D. Huang, X. Lin, L. Wang, and Y. Lv, "Performance evaluation of coherent free space optical communications with a double-stage fast-steering-mirror adaptive optics system depending on the greenwood frequency," *Opt. Exp.*, vol. 24, no. 12, pp. 13288–13302, Jun. 2016.

[16] H. Bai and S. Qu, "Relationship between system physics limits and system bandwidth," in *Proc. IEEE 4th Int. Conf. Control Sci. Syst. Eng.*, 2018, pp. 334–337.

[17] R. T. O'Brien, R. J. Watkins, and O. G. Thorp, "Cross-coupling estimation for optical beam stabilization," in *Proc. Amer. Control Conf.*, 2012, pp. 3944–3949.

[18] S. Tan, X. Yu, Y. Xu, Y. Xu, and P. Jia, "Micro-stress bonding analysis of high precision and lightweight mirrors," *Opt. Exp.*, vol. 29, no. 21, pp. 33665–33678, Oct. 2021.

[19] R. E. Walter, H. Danny, and J. Donaldson, "Stabilized inertial measurement system (SIMS)," in *Proc. Laser Weapons Technol. III*, 2002, vol. 4724, pp. 57–68.

[20] X. Zhou, H. Zhang, and R. Yu, "Decoupling control for two-axis inertially stabilized platform based on an inverse system and internal model control," *Mechatronics*, vol. 24, no. 8, pp. 1203–1213, 2014.

[21] J. Hilkert, "Inertially stabilized platform technology concepts and principles," *IEEE Control Syst. Mag.*, vol. 28, no. 1, pp. 26–46, Feb. 2008.

[22] H. Li, K. Han, X. Wang, S. He, Q. Wu, and Z. Xu, "A compact and lightweight two-dimensional gimbal for inter-satellite laser communication applications," *Opt. Exp.*, vol. 27, no. 17, pp. 24060–24071, Aug. 2019.

[23] M. Sweeney, L. Redd, T. Vettese, R. Myatt, D. Uchida, and D. Sellers, "Design and manufacturing considerations for high-performance gimbals used for land, sea, air, and space," in *Material Technologies and Applications to Optics, Structures, Components, and Sub-Systems II*, vol. 9574. Bellingham, WA, USA: SPIE, 2015, pp. 23–35.

[24] Y. Lin, Y. Ai, and X. Shan, "Identification of electro-optical tracking systems using genetic algorithms and nonlinear resistance torque," *Opt. Eng.*, vol. 56, no. 3, 2017, Art. no. 033105.

[25] T. Nakamura, S. Tani, I. Ito, M. Endo, and Y. Kobayashi, "Piezo-electric transducer actuated mirror with a servo bandwidth beyond 500 KHz," *Opt. Exp.*, vol. 28, no. 11, pp. 16118–16125, 2020.

[26] E. S. Ahn, R. W. Longman, J. J. K. Kim, and B. N. Agrawal, "Evaluation of five control algorithms for addressing CMG induced jitter on a spacecraft testbed," *J. Astronautical Sci.*, vol. 60, pp. 434–467, 2013.

[27] M. F. Luniewicz, J. P. Gilmore, T. T. Chien, and J. E. Negro, "Comparison of wideband inertial line-of-sight stabilization reference mechanizations," in *Proc. SPIE Int. Soc. Opt. Eng.*, 1992, vol. 1697, pp. 378–398.

[28] J. Lin, J. Tian, M. Lu, T. Ran, and J. Zhou, "Modeling and experimental analysis on the effect of carrier aircraft vibration on the imaging quality of an aspherical aerial camera," *Optik*, vol. 232, 2021, Art. no. 166571.

[29] Q. Deng, H. Feng, Z. Xu, Q. Li, Y. Chen, and W. Dong, "Study on MTF of remote sensing imaging under arbitrary known vibration," in *Proc. SPIE Int. Soc. Opt. Eng.*, 2012, vol. 8420, pp. 1–6.